Heavy and light inertial particle aggregates in homogeneous isotropic turbulence: A study on breakup and stress statistics

Graziano Frungieri[a,*], Matthäus U. Bäbler[b], Luca Biferale[c], Alessandra Sabina Lanotte[d]

[a]*Chair of Process Systems Engineering, TUM School of Life Sciences, Technical University of Munich*
[b]*Department of Chemical Engineering, KTH Royal Institute of Technology, Stockholm, Sweden*
[c]*Department of Physics and INFN, University of Tor Vergata, Rome, Italy*
[d]*CNR NANOTEC and INFN, Sez. Lecce, Lecce, Italy*

Abstract

The breakup of inertial, solid aggregates in an incompressible, homogeneous and isotropic three-dimensional turbulent flow is studied by means of a direct numerical simulation, and by a Lagrangian tracking of the aggregates at varying Stokes number and fluid-to-particle density ratio. Within the point-particle approximation of the Maxey-Riley-Gatignol equations of motion, we analyse the statistics of the time series of shear and drag stresses, which are here both deemed as responsible for particle breakup. We observe that, regardless of the Stokes number, the shear stresses produced by the turbulent velocity gradients similarly impact the breakup statistics of inertial and neutrally buoyant aggregates, and dictate the breakup rate of loose aggregates. When the density ratio is different from unity, drag stresses become dominant and are seen to be able to cause to breakup of also the most resistant aggregates. The present work paves the way for including the role of inertia in population balance models addressing particle breakup in turbulent flows.

Keywords: turbulent breakup, DNS, inertial aggregates, shear stress, drag stress, breakup rate

1. Introduction

Breakup of particles dispersed in a fluid flow is found at the core of many natural and engineering processes. For instance, in aquatic systems, the breakup of plastic waste governs the rate of microparticle production and, as such, plays a key role on the microplastics rate of release in the ocean (Garvey et al., 2020; Poulain et al., 2018; Brouzet et al., 2021). In some pharmaceutical applications, active particles are in need to be reduced in size before administration can take place (Capecelatro et al., 2022; Sabia et al., 2022; Vasquez Giuliano et al., 2022), and in polymer compounding processes, controlled breakup and redistribution of filler agglomerates is used to produce composites with enhanced mechanical and/or thermal properties (Frungieri et al., 2020b, 2022).

The breakup of dispersed particles is determined by a number of phenomena that challenges simple modelling approaches (Bäbler et al., 2008). The origin of this complexity relies on few main features: the first is the multi-scale nature of the problem, with relevant spatial scales ranging from the micron size of the particles to possibly hundreds of meters (the integral scale of the flow); the second is associated to the way aggregates spatially sample the flow, and the third depends on the complex interplay between fluid-induced stresses and inter-particle cohesive forces, which eventually governs the aggregate breakup dynamics.

Depending on the application of interest and degree of insight needed, different methods can be deemed as suitable to model breakup, and they can be mainly differentiated on the basis of the treatment of the dispersed and dispersing phase and in the mechanism taken into account to predict breakup (e.g. viscous shear, turbulent

---

*Corresponding author
Email address:* `graziano.frungieri@tum.de` (Graziano Frungieri)
[1]graziano.frungieri@tum.de, Tel: +49 8161 71-3788

fluctuations, wall impact, drag or rotary stress (Breuer & Khalifa, 2019)). On the scale of the aggregate, detailed predictions can be obtained by first principle structural mechanics (Zaccone et al., 2009; Conchúir & Zaccone, 2013; Jiang et al., 2020) or by Stokesian dynamics (Brady & Bossis, 1988), with the latter that, when coupled with models for the inter-particle interactions, is able to fully characterize the breakup occurrence in terms of critical stress and fragment size distribution. By such an approach, for instance, Harada et al. (2006) studied the effect of the internal connectivity on the aggregate breakup. Similarly, Harshe & Lattuada (2012) computed breakup rates and fragment size distribution in linear flows, and Frungieri & Vanni (2021) studied the particle size distribution and the morphological evolution of a population of colloidal particles at varying shear stress intensity and physico-chemical properties (Frungieri & Vanni, 2017; Frungieri et al., 2020a).

On the macro-scale (i.e., the scale of the equipment), where flow field heterogeneities and boundary layer phenomena affect the evolution of the dispersed phase, so called Eulerian-Eulerian approaches, especially when coupled with population balance models (Marchisio et al., 2006), are of particular interest, as they can be conveniently used to promptly compute the breakup dynamics and the particle size distribution. By such an approach a number of systems of practical relevance have been investigated, such as emulsions (Lebaz et al., 2021), bubbly flows (Syed et al., 2018; Zhang et al., 2021; Maluta et al., 2021; Lehnigk et al., 2022) and particle synthesis processes (Schikarski et al., 2022). However, despite the wide range of applications, such approaches still rely on empirical correlations, generally assuming a single phenomenon (e.g. viscous shear, turbulent fluctuations, surface instability) to be responsible for breakup, with the overall robustness of the approach still often in need to be checked against dedicated experimental campaigns.

More recently, approaches aimed at linking small scale and large scale phenomena have emerged, most of which adopted an Eulerian-Lagrangian simulation strategy. By such an approach, it is possible to study complex flow fields and treat in a more detailed way the dynamics of the dispersed phase, especially when the back-reaction of the particles on the flow is relevant. In this framework, Chen & Li (2020), considering an homogeneous isotropic turbulent flow, computed breakup rates in the early stage of an agglomeration process between adhesive particles, and single events such as restructuring and breakup by turbulent stresses were also studied (Ruan et al., 2020; Yao & Capecelatro, 2021). However, due to the high computational burden, this approach is limited to short simulated physical time, low level of turbulence (small turbulence Reynolds number Re_λ) and aggregates made by a small number of primary particles compared to what is typically observed in experiments (Saha et al., 2016).

Turbulence affects particle motion in a distinctive manner, in particular in the case of inertial particles (Brandt & Coletti, 2022). Inertia arises when particles have a finite size, and/or a density mismatch with the suspending medium. Because of inertia, particles show complex behaviours that notably affect their spatial distribution (Wang & Maxey, 1993; Bec et al., 2007) and their relative velocity and acceleration statistics (Falkovich & Pumir, 2007; Bec et al., 2011; Scatamacchia et al., 2012). In particular, strong inhomogeneities in the particles spatial distribution emerge, an effect that is maximal when the Stokes number is of order unity, and becomes negligible in the limits of both small and large inertia. Moreover, in the case of large inertia, heavy particles move almost independently of the fluid, hence they may collide with a large relative velocity. These events – dubbed *caustics* – can cause an substantial increase in the collision rate (Pumir & Wilkinson, 2016).

An attempt to understand how the properties of turbulence affect breakup was undertaken by Guseva & Feudel (2017) by evolving a population of particles of variable size in a synthetic turbulent flow. However, such a simulation method does not account for turbulence intermittency which is responsible for the generation of intense hydrodynamic stresses able to break also the strongest aggregates (Bäbler et al., 2015). In this context, Bäbler et al. (2012) computed the breakup rate of tracer-like aggregates at varying internal strength in a homogeneous isotropic turbulent flow, assuming particles to break under the action of the turbulent viscous dissipation only. Similarly, De Bona et al. (2014), by combining a DNS of the turbulent flow with a Discrete Element Method based on Stokesian dynamics, estimated the rate of breakup of aggregates addressing at the same time size and distribution of the formed fragments.

In this work, we study the fragmentation of inertial heavy and light aggregates in a turbulent flow by combining a direct numerical simulation of the turbulence with a Lagrangian tracking of the particles, perfomed within the point-particle approximation of the Maxey-Riley-Gatignol equations of motion. Likewise

to our previous work (Bäbler et al., 2012), we neglect the internal structure of the aggregates, the hydrodynamic interactions between them (Zahnow et al., 2011) and the accumulation of stresses on their structure (Marchioli & Soldati, 2015), and we assume breakup to occur whenever the local instantaneous hydrodynamical stresses acting on the aggregate exceeds a critical value (Bäbler et al., 2012; Breuer & Khalifa, 2019). We focus in particular on the role of the Stokes number and of the particle buoyancy on both shear and drag stresses and we evaluate the rate of breakup occurrence at varying aggregate strength.

The paper is organised as follows: in Section 2, we introduce the equation of motion for the inertial particles and the turbulent flow and we provide some details about their numerical integration; in Section 2.2, we present different approaches to measure the breakup rate. Results are discussed in Section 3, which are followed by the concluding remarks in Section 4.

2. Methodology

We consider a dilute suspension of aggregates described as point-like spherical particles, which have no feedback on the flow in which they are suspended, and which have no hydrodynamical interactions between them. Aggregates have sizes smaller or comparable to the Kolmogorov scale of the flow $\eta = (\nu^3/\langle\varepsilon\rangle)^{1/4}$, where ν is the kinematic viscosity of the fluid and $\langle\varepsilon\rangle$ is the mean rate of energy dissipation. Both the particle Reynolds number, defined as $Re_p = 2R\,v_p/\nu$, where v_p is a typical particle velocity and R the particle radius, and the particle Reynolds number based on the relative particle-fluid velocity, $2R|v_p - u_f|/\nu$, are small.

Aggregate trajectories are obtained by evolving a minimal formulation of the original Maxey-Riley-Gatignol equations of motion (Maxey & Riley, 1983; Gatignol, 1983) in which the pressure force, the added mass and the Stokes drag are kept into account, and which has been frequently used to describe the motion of small, rigid, spherical particles in unsteady flows (Bec et al., 2010). Such equations read as:

$$\frac{d\mathbf{X}}{dt} = \mathbf{V}(\mathbf{X}, t), \tag{1}$$

$$\frac{d\mathbf{V}}{dt} = \beta\frac{D\mathbf{u}(\mathbf{X}, t)}{Dt} + \frac{\mathbf{u}(\mathbf{X}, t) - \mathbf{V}(\mathbf{X}, t)}{\tau_p}, \tag{2}$$

where $\mathbf{V}$ is the particle velocity, $\mathbf{X}$ is the particle position and $\mathbf{u}$ is the undisturbed fluid velocity at the particle position. It is apparent that only two dimensionless parameters govern the particle motion: the density ratio β defined as $\beta = \frac{3\rho_f}{\rho_f + 2\rho_p}$ where ρ_p and ρ_f represent the particle and fluid density, respectively, and the Stokes number $St = \tau_p/\tau_\eta$, where the particle relaxation time is defined as $\tau_p = R^2/(3\beta\nu)$, being R the particle radius. The Kolmogorov time scale of the flow, entering the definition of the Stokes number, is $\tau_\eta = (\nu/\langle\varepsilon\rangle)^{1/2}$. From the definition of β, it is clear that neutrally buoyant particles have $\beta = 1$, extremely light particles have $\beta \to 3$, while heavy particles have $\beta \to 0$. We track the motion of particles at varying inertia, by changing both their buoyancy parameter and their Stokes number as schematically illustrated in Fig. 1.

The fluid velocity $\mathbf{u}$ is evolved according to the incompressible Navier-Stokes (NS) equations reading as:

$$\frac{\partial\mathbf{u}}{\partial t} + \mathbf{u}\cdot\nabla\mathbf{u} = -\frac{\nabla p}{\rho_f} + \nu\nabla^2\mathbf{u} + \mathbf{F}, \qquad \nabla\cdot\mathbf{u} = 0. \tag{3}$$

A steady, statistically homogeneous and isotropic turbulent flow is obtained by adding to the NS equations a forcing term $\mathbf{F}$ injecting energy in the first low-wave number shells and keeping constant their spectral content (Bec et al., 2010). The kinematic viscosity is chosen in such a way that the Kolmogorov length scale equals the grid spacing $\eta \simeq \delta x$. By doing so, a good resolution of the small-scale velocity fluctuations is obtained. At the steady state, the energy input balances the mean kinetic energy dissipation such that $\langle\mathbf{F}\cdot\mathbf{u}\rangle \simeq \langle\varepsilon\rangle$. The Navier Stokes equations are solved on a 512^3 cubic grid with periodic boundary conditions and a Taylor–Reynolds number $Re_\lambda \simeq 185$. In Table 1 the main characteristics of the flow are reported. Further numerical details on both the Eulerian and Lagrangian approaches can be found in the work by Bec et al. (2010).
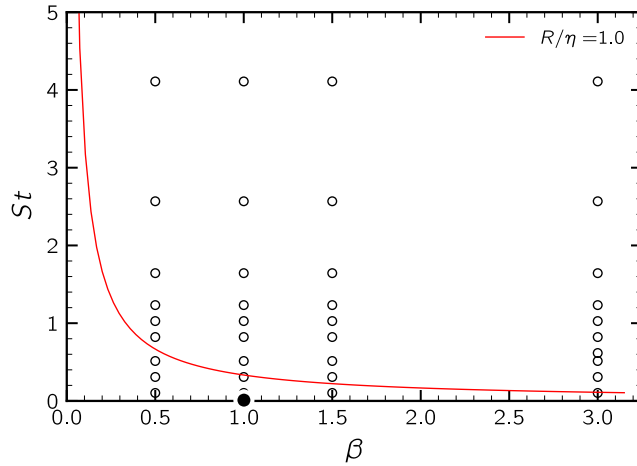
Figure 1: Parameters space of the particles used in our numerical experiments. The red line represents the locus of constant R/η. We analyzed $128k$ trajectories per each single (β, St) choice. Tracers are represented by the black dot. Trajectories were evolved using a second order algorithm, with a time step dt such that $\tau_\eta \simeq 100 dt$.

Table 1: Parameters of the DNS simulation. Microscale Reynolds number Re_λ, root-mean-square velocity u_{rms}, mean energy dissipation ε, kinematic viscosity ν, Kolmogorov scale $\eta = (\nu^3/\langle\varepsilon\rangle)^{1/4}$, integral scale L, Eulerian large-eddy turnover time $T_E = L/u_{\mathrm{rms}}$, Kolmogorov timescale $\tau_\eta = (\nu/\langle\epsilon\rangle)^{1/2}$, grid spacing Δx, number of grid points N, simulation time t_s.

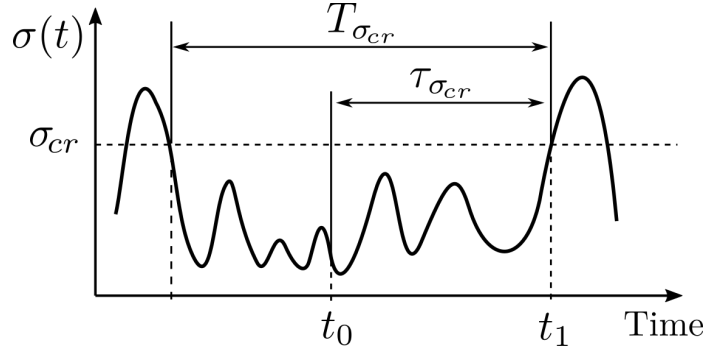| Re_λ	u_{rms}	ε	ν	η	L	T_E	τ_η	Δx	N^3	t_{s}
185	1.4	0.94	0.00205	0.010	π	2.2	0.047	0.012	512^3	13.2

4

Figure 2: Schematic of the total hydrodynamic stress along a particle trajectory. The particle is released at time t_0 and breaks up at time t_1. The time-lags $\tau_{\sigma_{cr}}$ and $T_{\sigma_{cr}}$ are the exit time and the diving time, respectively.

2.1. Hydrodynamic stresses

Once a statistically steady state condition in the flow is reached, particles are released at random in the fluid, and the time-series of the hydrodynamic stresses acting on them is tracked. We assume aggregates to be brittle objects that instantaneously respond to the external stress and that undergo breakup as soon as their critical resistance is exceeded by the total fluid dynamic stress acting on them.

Following Kusters (1991) and Breuer & Khalifa (2019)), two hydrodynamic stresses are deemed as responsible for the breakup of the aggregate, namely the shear stress σ_ε, due to the fluid velocity gradients at the particle position, and the drag stress σ_{St}, due to the slip velocity between the particle and the underlying flow. The first is evaluated along the particle trajectory $\mathbf{X}$ as:

$$\sigma_\varepsilon(\mathbf{X}, t) = \mu \sqrt{\frac{2}{15} \frac{\varepsilon(\mathbf{X})}{\nu}}, \tag{4}$$

where $\mu = \nu \rho_f$ is the dynamic viscosity of the flow, and where the local turbulent dissipation rate was computed as $\varepsilon = 2\nu e_{ij} e_{ij}$, being $e_{ij} = 1/2(\nabla_j u_i + \nabla_i u_j)$ the symmetric part of the velocity gradient tensor $\nabla_j u_i$.

The drag stress is instead evaluated as:

$$\sigma_{St}(\mathbf{X}, t) = \mu \frac{3|\mathbf{u}(\mathbf{X}) - \mathbf{V}(\mathbf{X})|}{2R}. \tag{5}$$

where we have assumed, as above, that the stress is isotropic and that the aggregate has a spherical shape (see also Breuer & Khalifa (2019) for a discussion). Therefore the drag stress acting on an aggregate can be simply computed as the ratio between the drag force $6\pi\mu R|\mathbf{u} - \mathbf{v}|$ and the surface area $4\pi R^2$. Following Kusters (1991), the two stresses are added up linearly $\sigma_{tot} = \sigma_{St} + \sigma_\epsilon$, thus assuming that the two stresses propagate instantaneously across the aggregate bond network and that their load on the structure can be superimposed.

2.2. Breakup rate measurements

Our work is aimed at evaluating particle breakup rates at varying inertia. In our model, an individual aggregate undergoes breakup instantaneously when the total hydrodynamic stress acting on it exceeds a critical threshold value σ_{cr}, representing the aggregate mechanical strength.

Figure 2 illustrates the simple modeling framework we use. The aggregate is released at a random time t_0 and samples the flow until it experiences for the first time a hydrodynamic stress exceeding its resistance σ_{cr} (this, in the schematics of Fig. 2, occurs at t_1). The time-lag between release at t_0 and breakup at t_1 identifies the exit time $\tau_{\sigma_{cr}}$. The breakup rate is therefore calculated as the inverse of the mean exit time, i.e., as:

$$f_{\sigma_{cr}} \equiv \frac{1}{\langle \tau_{\sigma_{cr}} \rangle}. \tag{6}$$

5

Notice that within this modelling framework, situations where the hydrodynamic stress exceeds the critical stress already at the point of release are ignored when computing the average in Eq. (6). The reason for this is that breakup events that occur right at the point of release would be governed by the frequency of aggregate release and not by the timescale of the turbulent fluctuations.

The picture presented in Fig. 2 can be used to identify a second time scale. For this, we notice that the hydrodynamic stress experienced by the aggregate during its lifetime is part of the Lagrangian time series of a particle with the same kinematic characteristics (Stokes number and density parameter) as the aggregate. Since this Lagrangian time series exists throughout the lifetime of the flow, the hydrodynamic stress can also be traced backwards in time, as depicted in Fig. 2. Hence, by considering the Lagrangian time series of which the aggregate released at t_0 sampled the segment between t_0 and t_1, we can identify a new time scale, called diving time $T_{\sigma_{cr}}$, as the time-lag between the last down-crossing of σ_{cr} before t_0 and the first up-crossing of σ_{cr} after t_0. This time scale $T_{\sigma_{cr}}$ allows us for deriving a few additional relationships to express or approximate the breakup rate. At first, it can be shown that for a statistically stationary flow the breakup rate defined in Eq. (6) can also be expressed through the variance of the diving time as (Bäbler et al., 2012):

$$f_{\sigma_{cr}} = \frac{2\langle T_{\sigma_{cr}} \rangle}{\langle T_{\sigma_{cr}}^2 \rangle} \tag{7}$$

Moreover, we can define a proxy-breakup rate by using the diving time instead of the exit time. The proxy-breakup rate simply reads as:

$$\tilde{f}_{\sigma_{cr}} = \frac{1}{\langle T_{\sigma_{cr}} \rangle} \tag{8}$$

For a stationary stochastic process, the above can be calculated by the frequency of upward-crossing of the the threshold σ_{cr} divided by the fraction of time the trajectory stays below the threshold. The former can be expressed by means of the Rice theorem, whereas the latter follows from the probability density function (PDF) of $\sigma_{tot}(t)$ (Lindgren, 2019). By doing so, the proxy-breakup rate can be computed as:

$$\tilde{f}_{\sigma_{cr}} = \frac{\int_0^\infty d\dot{\sigma}_{tot}\, \dot{\sigma}\, p_2(\sigma_{cr}, \dot{\sigma}_{tot})}{\int_0^{\sigma_{cr}} d\sigma_{tot}\, p(\sigma_{tot})} \tag{9}$$

where $p_2(\sigma_{tot}, \dot{\sigma}_{tot})$ is the joint PDF of the total stress and of its time derivative, and where $p(\sigma_{tot})$ is the PDF of σ_{tot}. Approximating the breakup rate using the Rice formula was first proposed by Loginov (1986). Accordingly, Eq. (9) is referred to as Loginov's approximation.

For large values of the threshold σ_{cr}, the proxy-breakup rate based on the diving time (Eq. (8)) approaches the exact breakup rate based on the exit time (Eq. (6)):

$$\langle \tau_{\sigma_{cr}} \rangle \sim \langle T_{\sigma_{cr}} \rangle \quad \text{for} \quad \sigma_{cr} \gg \langle \sigma_{tot} \rangle \tag{10}$$

To understand this, let us consider a long timeseries of length t_L, with t_L being much larger than the large eddy turnover time T_E. Along this time series, the threshold σ_{cr} is crossed N-times in the upward direction. Since the threshold is very large, the total time the timeseries spends above σ_{cr} is negligible and the mean diving time follows as $\langle T \rangle = t_L/N$. To connect this to the exit time, we assume that the up-crossings of σ_{cr} are distributed randomly along the trajectory. Considering that the timespan between two consecutive upcrossings is large compared to the large eddy turnover time T_E, this assumption is reasonable.

Next to the N upward-crossing events along the trajectory, there is now also another event i.e., the release of the aggregate at a random time t_0, such that in total there are $N + 1$ events along the trajectory. Thus, the mean exit time follows as $\langle \tau \rangle = t_L/(N + 1)$. For a stationary flow, the length t_L and the number of upward-crossings N are large such that $t_L/N \approx t_L/(N + 1)$, finally rationalizing the result of Eq. (10).
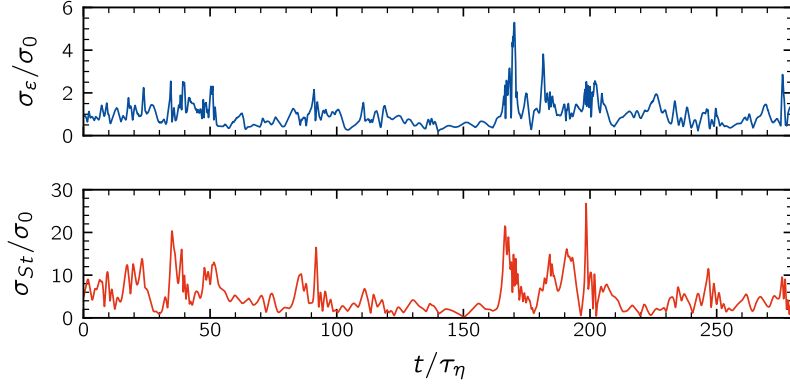
Figure 3: Time series of the shear stress σ_ε (top panel) and drag stress σ_{St} (bottom panel) for a sample aggregate with Stokes number $St = 1.64$ and buoyancy parameter $\beta = 3$. The x axis is normalized by the Kolmogorov time scale of the flow. The y-axis is normalized by the average shear stress σ_0 experienced by tracer particles ($\beta = 1$, $St = 0$).
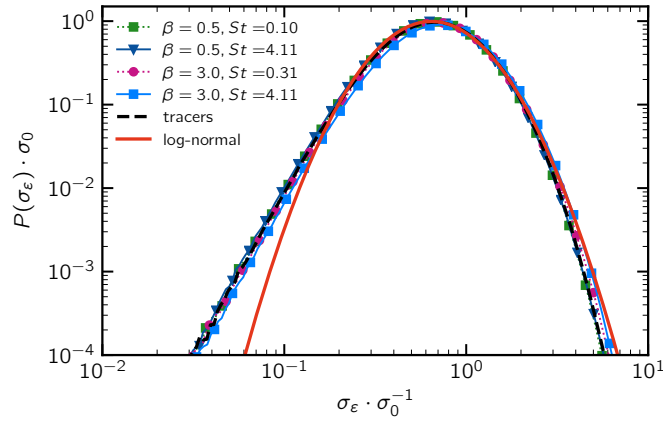

Figure 4: Probability density function of the shear stress at varying particle inertia. The red dotted line represents a log-normal distribution $P(\sigma_0, 0.55\sigma_0)$, with σ_0 being the average σ_ε experienced by tracer particles.

3. Results and discussion

3.1. Hydrodynamic stress statistics

To study the statistics of the hydrodynamic stresses experienced by inertial aggregates, we start by consider them as infinitely strong and moving in the flow field without undergoing breakup. Figure 3 shows the time series of the shear stress σ_ε and of the drag stress σ_{St}, recorded along the trajectory of a heavy aggregate with inertia values $\beta = 0.5$ and $St = 1.64$. We observe that both stresses exhibit strong fluctuations, each with its own dynamics. Indeed, the first is determined by the way the particle sample the different regions of the flow, whereas the second comes from the fluid-particle slip velocity. For the chosen set of inertia parameters, we also observe that the drag stress dominates over the shear stress along the whole particle trajectory. Figure 4 reports the probability density function of the shear stress for two buoyancy parameters ($\beta = 0.5$ and $\beta = 3.0$, corresponding to heavy and light particles, respectively) and for the smallest and largest Stokes values here investigated. The plot also reports the distribution of the shear stress experienced by tracer particles, for which $\beta = 1$ and $St \to 0$. It is apparent that, for all combination of β and St, the curves are very similar and, more remarkably, regardless of their inertia, all particles sample the shear stress field exactly as tracer particles do, as it is made apparent by the fairly good overlap of the distributions within the whole stress range.
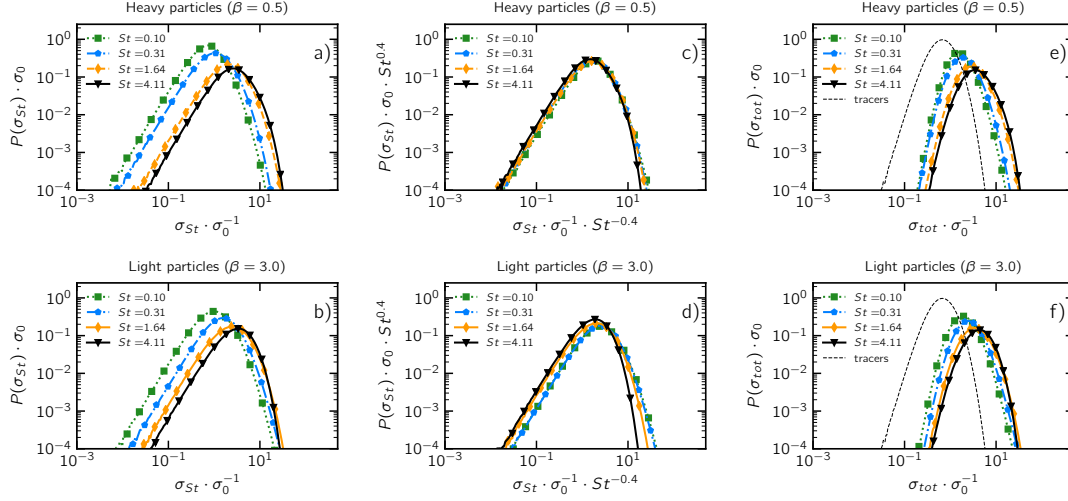
7

Figure 5: Probability density function of the fluid dynamic stresses for heavy and light particles at varying Stokes number. Panel a) and b) report the PDFs of the drag stress. In panel c) and d) the same PDFs are rescaled by $St^{0.4}$. Panel e) and f) report the total stress distributions. In these two panels, the black dotted line is the PDF of the shear stress experienced by tracers.

Furthermore, the shear stress σ_ε appears to be well fitted, at least for the central part of the value range, by a log-normal distribution peaking at the average value of the shear stress σ_0 experienced by tracers.

Figures 5a) and b) show the PDF of the drag stress for heavy and light particles, respectively, at varying Stokes number. In these two panels the PDFs are shown in dimensionless coordinates, without scaling. The average values of the drag stress for a larger set of particle properties are shown in Fig. 6a), where it is apparent that the average drag stress increases with the Stokes number. To better understand the general behavior, we recall that the drag stress is proportional to the slip velocity $|\mathbf{u} - \mathbf{V}|$ (see Eq. (5)).

In Fig. 6b), we show the normalised average slip velocity as a function of both the Stokes number and the buoyancy parameter: at small Stokes number, we observe that the mean slip velocity scales linearly for all the investigated buoyancy parameters, in agreement with the Maxey approximation for weak inertia (Maxey, 1987). Indeed, starting from Eq. (2), in the limit of $St \to 0$, the slip velocity becomes:

$$\mathbf{u} - \mathbf{V} \equiv \tau_p \left(d\mathbf{V}/dt - \beta D\mathbf{u}/Dt \right) \simeq \tau_p (1 - \beta) a_f, \tag{11}$$

where we have assumed that in the limit of small Stokes numbers the aggregate acceleration and the fluid acceleration along the aggregate trajectory are equal, i.e., $d\mathbf{V}(\mathbf{X})/dt \simeq D\mathbf{u}(\mathbf{X})/Dt \simeq a_f(\mathbf{X})$. Hence, in the weak inertia limit, $\langle|\mathbf{u} - \mathbf{V}|\rangle \propto St$ (Boffetta et al., 2007) as shown by the dotted line in Fig. 6b.

However, we also observe that the mean slip velocity can be described fairly well by the power-law scaling $\langle|\mathbf{u} - \mathbf{V}|\rangle \simeq St^\alpha$, with $\alpha = 0.9$: in other words, an *effective* and *empirical* exponent, α, can be introduced that models the slip velocity behaviour over a wide range of Stokes numbers (up to $St \sim O(1)$). Such an exponent is found to be independent, or weakly dependent, on the buoyancy parameter. Recalling that the drag stress $\sigma_{St} \propto |\mathbf{u} - \mathbf{V}|/R$, and that $R \propto O(St^{1/2})$, we finally obtain that $\sigma_{St} \propto St^{0.4}$. If we apply this scaling to the probability distribution functions of the drag stress of Figs. 5a,b), we observe that the distributions collapse onto a single curve for both light particles (up to $St \approx 1.64$) and heavy particles (up to $St \approx 4.11$) over a quite wide range of σ_{St} (see Figs. 5c,d). We also note that the left tail of the drag stress is well described by a χ^2 distribution with 3 degrees of freedom. We consider this an outcome of the Gaussian dynamics of the smallest stress contributions. To summarise, the collapse of the left tails of the PDFs is clearly a consequence of the fact that small fluctuations of the slip velocity are proportional to the first moment of the distribution, as expected; moreover, these small fluctuations occur in the smooth regions of the flow.

The panels e) and f) in Fig. 5 show the probability distribution functions of the total stress for heavy and
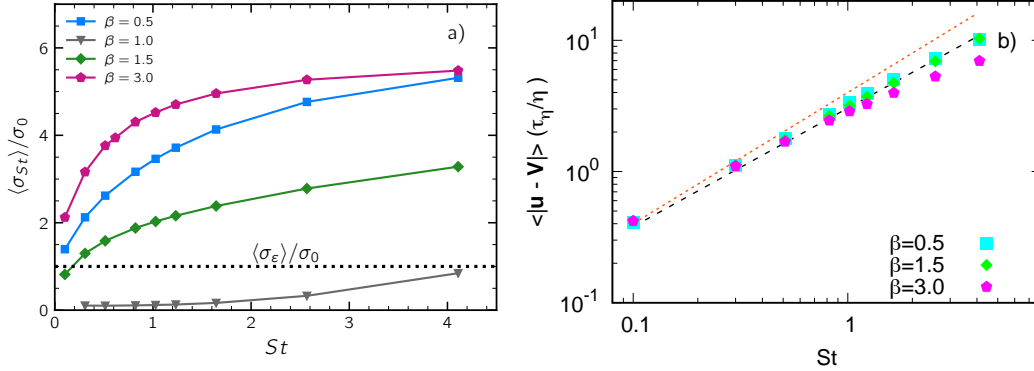
8

Figure 6: a) Drag stress for various β values as a function of St. The dotted line reports the average σ_ε experienced by tracers. b) Log-log plot of the fluid-particle slip velocity as a function of the Stokes number, for various β values. The slip velocity is made dimensionless by the Kolmogorov time η and length scale τ_η; for $\beta = 0.5$ and $\beta = 1.5$, the slip velocity have been shifted vertically for plotting purposes. The red dotted line shows the theoretical scaling in the limit of small Stokes number $\langle |\mathbf{u} - \mathbf{V}| \rangle \propto St$; while the black dashed line shows the scaling $\langle |\mathbf{u} - \mathbf{V}| \rangle \propto St^{0.9}$.

light particles. The distribution of the shear stress experienced by tracers, which, as already discussed, is very similar to the one of the other particle families, is also reported for comparison. The shifting of the curves towards the right at increasing St makes it apparent that, as inertia is increased, particles experience larger drag stresses. However, at Stokes number ≈ 4, a drop down in the probability of the largest stresses can be observed, especially for light particles.

Even if particles experience the shear stress space in a way similar to the one of tracers, when looking at the statistics of the experienced flow topology, important differences emerge. We characterize the flow topology along particle trajectories according to the mixing index λ, defined as:

$$\lambda = \frac{\sqrt{II_{\mathbf{E}^\infty}}}{\sqrt{II_{\mathbf{E}^\infty}} + \sqrt{II_{\mathbf{\Omega}^\infty}}} \tag{12}$$

where $II_{\mathbf{E}^\infty}$ is the second invariant of the rate-of-strain tensor $\mathbf{E}^\infty$ and where $II_{\mathbf{\Omega}^\infty}$ is the second invariant of the vorticity tensor $\mathbf{\Omega}^\infty = 0.5 \left(\nabla \mathbf{u}^\infty - \nabla \mathbf{u}^{\infty,T} \right)$. The mixing index has a 0–1 range, with 0 indicating a pure rotational motion, and 0.5 and 1 indicating pure shear and pure elongational flow, respectively. Figure 7a) reports the average mixing index λ seen by the aggregates for different Stokes numbers and buoyancy parameter β. The black dot at $\lambda = 0.55, St = 0$ indicates the behavior of tracers. The plot makes apparent that, regardless of the β parameter, small Stokes aggregates behave very similarly to tracer aggregates with an average mixing index fairly close to 0.55. However, as the Stokes number increases, qualitative differences can be observed. Neutrally buoyant aggregates ($\beta = 1$) keep behaving as tracer aggregates, with the average λ almost constantly equal to 0.55 at increasing St. On the contrary, heavy and light aggregates show two different behaviors: the heavy aggregates ($\beta = 0.5$) present a maximum in $\langle \lambda \rangle$ for $St \approx 1$ and converge to the tracers behaviour again as Stokes increases.

Light aggregates ($\beta = 1.5$ and $\beta = 3$), on the contrary, have a minimum $\langle \lambda \rangle$ at $St \approx 1$, which is kept almost constantly up to $St = 4$. This confirms what already pointed out by other researchers (Calzavarini et al., 2008b,a), who observed that light aggregates preferentially sample the vortical regions of the flow (i.e., lower λ regions), whereas heavy aggregates are ejected from vortical regions and tend to sample the higher strain regions (larger λ). This behavior, referred to as *turbulence induced segregation*, is here observed to be particularly important at $St \approx 1$, in line with what reported by Bec et al. (2005). Finally, to make this behavior more apparent, Fig. 7b) reports the joint probability distribution functions of the mixing index and turbulent dissipation rate ε for two different aggregates classes, with same Stokes number ($St \approx 1$) and different β parameters, and for tracers. It is again apparent that all aggregates sample almost equally the ε space, but quite differently the λ space: heavy aggregates experience the larger values of the λ range and behave more
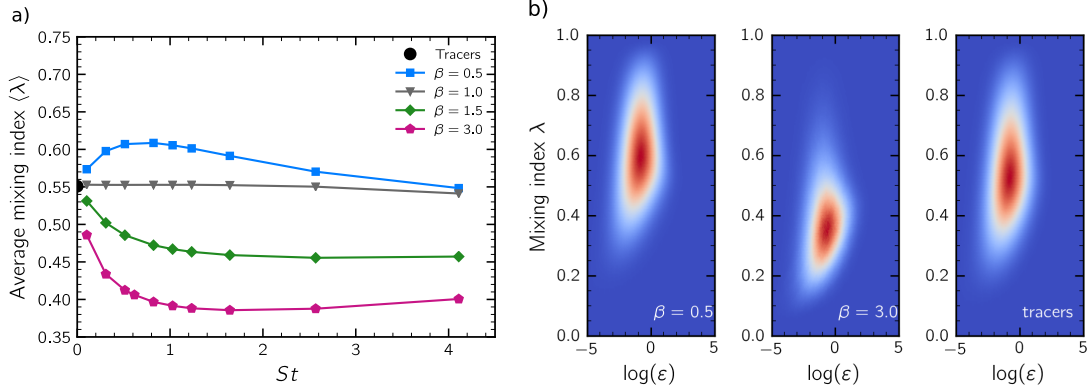
9

Figure 7: a) Average mixing index seen by aggregates as a function of both St and β. The black circle indicates the tracer behavior. b) Bivariate distribution function of the turbulent dissipation rate and mixing index for heavy aggregates ($\beta = 0.5$), light aggregates ($\beta = 3$) and tracers. Stokes number is approximately equal to 1 for both the light and the heavy aggregate class.

similarly to tracers, except for the lower amplitude of the fluctuations in the λ direction; light aggregates ($\beta = 3$) sample the lower value range of the mixing index and experience smaller fluctuations. This confirms that are more preferably trapped in the vortical regions of the flow.

3.2. Breakup statistics

Figure 8 shows the breakup rate as a function of the threshold stress for two particle families with same Stokes number ($St = 4.11$) and different buoyancy parameters, namely $\beta = 0.5$ (panel a) and $\beta = 3$ (panel b). The threshold stress on the horizontal axis is normalized by the mean shear stress σ_0 and the breakup rate is normalized by the Kolmogorov time scale τ_η. Although the data shown refers to particle families on the outskirts of our dataset (see Fig. 1), the graph reflects the general trend of the breakup rate and allows us for discussing its characteristics and the different approaches used for measuring it. As the total stress is calculated from the three components of the slip velocity and from the spatial derivatives of the fluid velocity, that are both quantities that fluctuate along a particle trajectory, the exit time has to be considered as an outcome of a combination of random variables. For small threshold values, this combination leads to a breakup rate following a power-law behavior: in this regime, in fact, breakup events are controlled by hydrodynamic stresses that are close to the mean stress and occur in the smooth regions of the flow, where the stress statistics are Gaussian distributed.

However, as the threshold increases, the breakup rate has a sudden super-exponential drop-off. This behaviour is the consequence, on the contrary, of the rare turbulent events that are vigorous enough to break strong aggregates, whose occurrence is controlled instead by turbulent intermittency.

Regarding the different approaches for measuring the breakup rate, it is observed that for small threshold values the exact breakup rate based on the exit time (square symbols) is very close to the proxy-breakup rate based on the diving time, that in Fig. 8 is shown by both its discrete measurement (star symbols) and its analytical extension provided by the Loginov's formula (line). To understand this similarity we analyze the PDFs of the exit time and of the diving time. Figure 9a) shows the PDF of the diving time for the same particle family as shown in Fig. 8a) and for two threshold values. We observe that the PDF has a sharp decrease for small diving times followed by a well developed exponential tail. The presence of the exponential tail implies that the realization of diving events whose duration exceeds the correlation time of the hydrodynamic stress can be described as a Poisson process, where individual diving events are independent of each other. Moreover, an exactly exponentially distributed diving time would lead to an equivalence of the mean diving time and the mean exit time, i.e. $\langle T \rangle = \langle \tau \rangle$ (this follows from using $p(T) \sim e^{-t/\langle T \rangle}$ in Eq. (7)). However, the deviations from the exponential distribution for short diving events, that are particularly pronounced for the intermediate values of the threshold shown in Fig. 9, result in the diving time being different from the
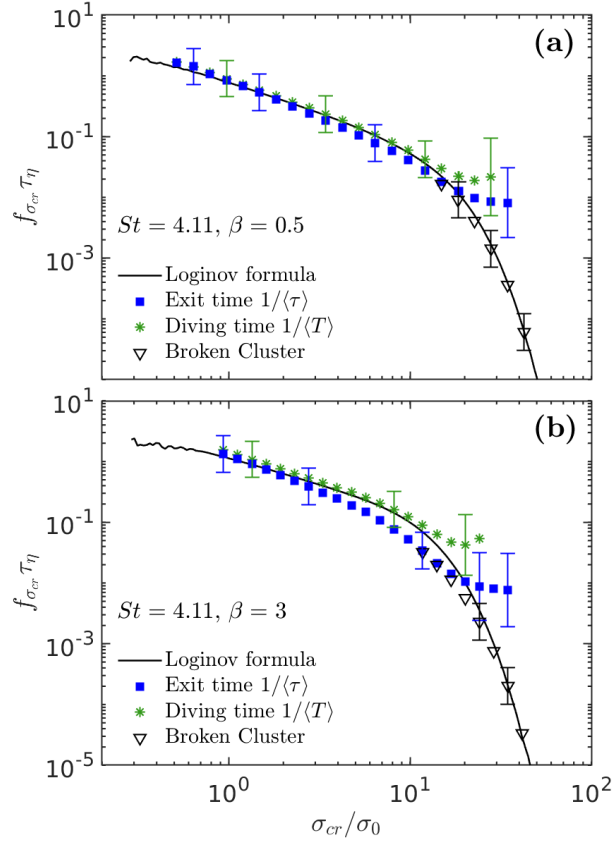
Figure 8: Breakup rate versus the threshold stress for aggregates with $St = 4.11$ and (a) $\beta = 0.5$ and (b) $\beta = 3$ measured by the exact expression based on the exit time (square symbols) and the approximations based on the diving time (star symbols), broken clusters (triangles) and the Loginov formula (lines). The horizontal axis is normalized by the mean shear stress σ_0, whereas the vertical axis is normalized by the Kolmogorov time scale τ_η. For the sake of clarity, error bars are shown for few data points only.
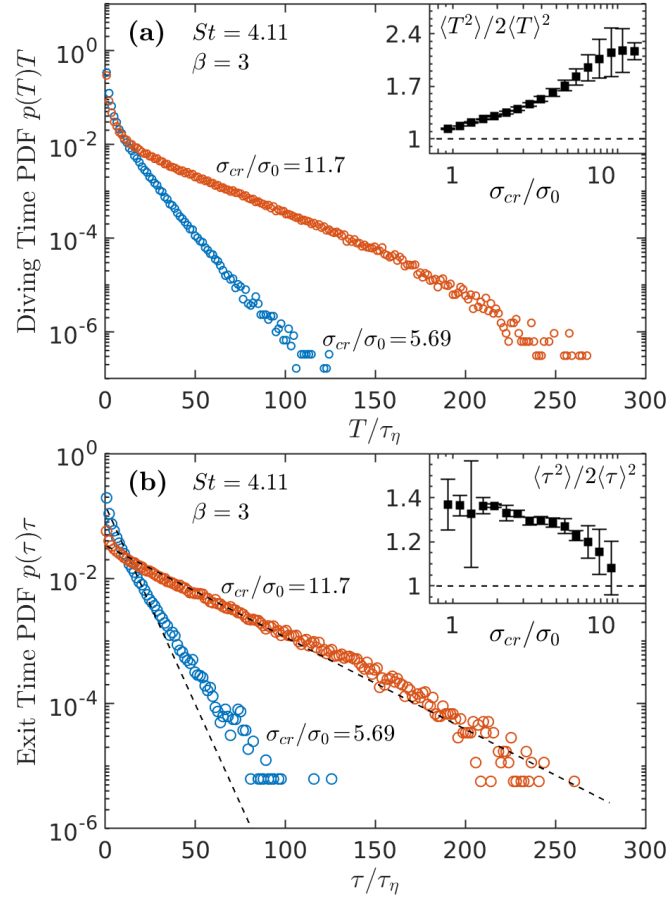
Figure 9: Probability density function for aggregates with $St = 4.11$ and $\beta = 3$ of (a) the diving time and (b) the exit time at two critical stress values. The dashed lines in (b) show exponential distributions with an expected value equal to the mean exit time for the given threshold. The insets show the normalized second order moment of the diving time and the exit time as a function of the critical stress.

exit time. These deviations for short diving times reflect the correlation of short-lived turbulent fluctuations, i.e. the burst in turbulent intensity which often come with multiple spikes in the stress intensity, as visible in Fig. 3. To quantify the deviation from an exponential distribution we report in the inset of Fig. 9a) the moment ratio $\langle T^2 \rangle / (2 \langle T \rangle)$. For an exponential distribution, this moment ratio has a value of unity. As it can be seen, the moment ratio for the diving time is larger than one. This has indeed to be ascribed to the sharp drop of the diving time PDF for short diving times.

Returning to Fig. 8, we note that for large thresholds values, for which breakup is governed by the rare and intense turbulent events, there are not enough statistics to measure the mean exit and mean diving time with confidence. In other words, the length of exit and diving events becomes comparable or larger than the run-time of our simulation. This causes the data for the breakup rate based on the exit time (solid squares) and on the diving time (star symbols) to level off or even to increase. Inspection of the underlying PDFs reveals that this is an artefact caused by the finite run time of our simulation. In comparison, the Loginov's formula (solid line) keeps on decaying, thus giving the more realistic picture.

To independently estimate the breakup rate for large threshold values (and thus to validate the Loginov formula) we make use of another routine. This consist of releasing a large number of aggregates at the beginning of the simulation and monitoring the decay of their number concentration as breakup events occur. From the temporal evolution of the number of aggregates $N(t)$ we can estimate the breakup rate assuming a first-order process as:

$$\frac{dN}{dt} = -\hat{f}_{\sigma_{cr}} N \tag{13}$$

On the basis of Eq. (13), the proxy breakup rate can be determined from the slope of a plot of $\ln(N/N_0)$ versus t. The first order process given by Eq. (13) assumes that the events that cause breakup (i.e. the intense fluctuations in the hydrodynamic stress) are independent from each other. Moreover, the dynamics underlying Eq. (13) is equivalent to an exit time that has an exponential distribution. This is explored in Fig. 9b) that shows the PDF of the exit time for two threshold values. It is seen that the exit time is approximately exponentially distributed, with small deviations at short exit times, and at small threshold values for large exit times. To assess the deviations from exponential distribution in the inset of Fig. 9b) we show the normalized second order moment of the exit time, i.e $\langle \tau^2 \rangle / (2 \langle \tau \rangle)$, as a function of the threshold stress. For an exponential distribution, the normalized second order moment has a value of unity. As it can be seen, at increasing threshold stress, the normalized second order moment approaches one, implying that the exit time PDF comes closer to an exponential distributions and hence, the dynamics proposed by Eq. (13) become more accurate. This latter observation is also confirmed by the breakup rate in Fig. 8. The open triangle symbols show the estimate based on the Eq. (13), from which see that, for intermediate threshold values, for which both the exit time measurement and the concentration decay can be measured with confidence, we find good agreement between the two. Moreover, for large threshold values the estimate based on the concentration decay (open triangles) is in agreement with the Loginov's formula (lines), a result which is in line with Eq. (10). Based on these findings, in the following, we will report the breakup rate in terms of the exact expression based on the exit time for small and intermediate thresholds, that is for breakup rates $f_{\sigma_{cr}} \tau_\eta > 0.01$, whereas for large thresholds we will report the estimate from the decaying particle concentration of Eq. 13.

3.3. Breakup rate of inertial aggregates

Figure 10 shows the breakup rate as a function of the threshold stress for neutrally buoyant aggregates with varying Stokes number. Lines refer to the proxy-breakup rate based on the Loginov's formula of Eq. (9), whereas symbols refer to direct measurements based on the exit time (Eq. (6); square symbols) and on the concentration decay (Eq. (13); triangle symbols). The data shows a clear shift in the breakup rate, i.e., we observe a transition from a shear dominated breakup mechanism at $St = 0$ to a drag dominated one as St becomes large. Shear stresses are relatively weak and, accordingly, only weak aggregates are broken down by shear. This is the reason why an early drop-off of the breakup rate occurs for tracer-like aggregates. For instance, this makes a tracer-like aggregate of strength $\sigma_{cr} \sim 10 \, \sigma_0$ very hard to break.
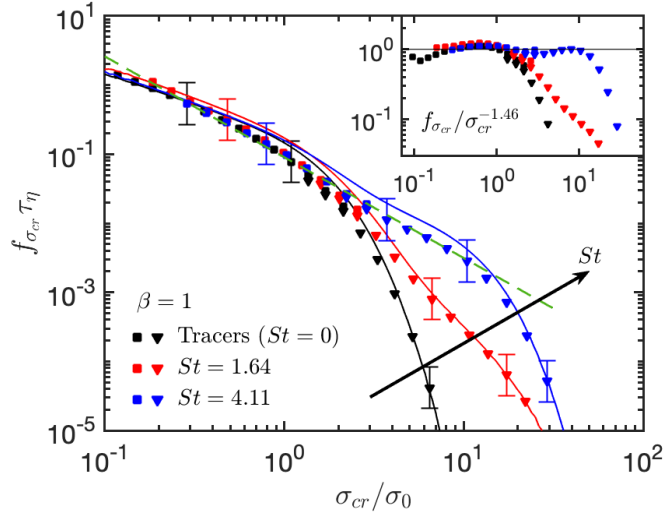
13

Figure 10: Breakup rate as a function of the threshold stress for $\beta = 1$ and three different Stokes numbers measured by the exact expression based on the exit time (square symbols) and on the broken cluster approach (triangles). Solid lines report the breakup rate measured by the Loginov's formula. The dashed line shows the fitted power-law expression $f_{\sigma_{cr}} \sim \sigma_{cr}^{-k}$, with $k = 1.46 \pm 0.04$. The inset shows the breakup rate compensated by the power-law expression.

As the Stokes number increases, the slip velocity grows and gives origin to an additional drag stress acting on the aggregate. This stress causes a shift of the drop-off of the breakup rate towards larger threshold values, such that in this case an inertial aggregate with strength $10\,\sigma_0$ has a substantial breakup frequency, as made apparent by the two non-tracer curves in Fig. 10.

It is interesting to notice that despite the additional contribution of the drag stress, the power-law part of the breakup rate is not affected by inertia, i.e., for small threshold stresses, the breakup rates for neutrally buoyant aggregates collapse to a single master curve following a power-law of the form $f_{\sigma_{cr}}/\tau_\eta = 0.090\,(\sigma_{cr}/\sigma_0)^{-k}$, where $k = 1.46 \pm 0.04$, as shown by the dashed curve in Fig. 10. The inset of Fig. 10 shows the breakup rate compensated by this power-law expression, underlining the quality of the power-law master curve.

The breakup rate for heavy and light aggregates is shown in Fig. 11. For these aggregates, the drag stress is dominant and causes a shift of the breakup rate towards higher threshold stresses at already small Stokes number. For instance, at the smallest Stokes number reported ($St = 0.31$) drag stresses already exceed the shear stresses by an order of magnitude, thus determining the observed shift of the breakup rate towards the right. As the Stokes number further increases, the breakup rate for both heavy and light aggregates saturates. For heavy particles ($\beta = 0.5$, Fig. 11a)) the breakup rate reaches an apparent maximum. This maximum (made apparent by the overlap of the curves for $St = 1.64$ and $St = 4.11$ in Fig. 11a) follows again a power-law for the small threshold values and has a sharp super-exponential cut-off at larger thresholds. For light particles ($\beta = 3$, Fig. 11)) the overlap at large Stokes numbers is less pronounced and we even observe a reduction in the breakup rate for large threshold stresses and large Stokes numbers. This sharper drop-off at $St = 4.11$ well agrees with the PDFs of the total stress reported in Fig. 5f). Careful inspection of the PDFs reveals in fact a slightly wider right tail at intermediate Stokes numbers (i.e. $St = 1.64$) compared to the largest Stokes number studied in our work ($St = 4.11$). This implies that large excursions of the total stress are more frequent for intermediate Stokes numbers than for large Stokes numbers, i.e., light particles with large Stokes number exhibit a mild filtering effect that prevents them from experiencing high drag stresses, thus causing the sharper cut-off of the breakup rate for $St = 4.11$ visible in Fig. 11b.
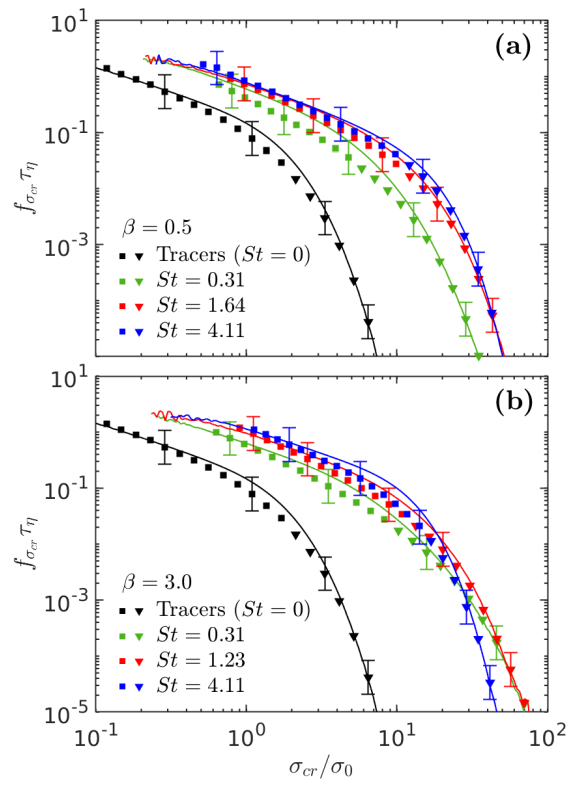
14

Figure 11: Breakup rate for varying particle critical stress. Data refer to heavy aggregates with $\beta = 0.5$ (a) and light aggregates with $\beta = 3.0$ (b).

4. Conclusions

In this work we have studied the stress and breakup statistics of inertial aggregates in homogeneous isotropic turbulence, at varying fluid-to-particle density ratio and Stokes number. We have solved the flow dynamics by a direct numerical simulation and tracked the particles trajectories by evolving a minimal formulation of the Maxey-Riley-Gatignol equation. We have deemed both shear stress and drag stress as responsible for the particle breakup and we have assumed breakup to occur in a brittle manner, i.e., aggregates break instantaneously when they experience a fluid dynamic stress larger than their mechanical resistance. We have devised and tested different approaches for measuring the breakup frequency, discussing in detail their theoretical foundations and limitations.

Two distinct breakup regimes exist, depending on the aggregate mechanical strength. Loose aggregates have large breakup frequencies and are broken down in the smooth regions of the flow, where the stresses are Gaussian distributed, thus making the breakup frequency to follow a power-law behaviour with the aggregate strength. Conversely, strong aggregates have lower breakup rates and are broken down by the burst of the hydrodynamic stresses, which are dictated by the turbulent intermittency.

Results have also shown that inertial effects have a major role in determining breakup rates. When inertial effects are limited (i.e., for neutrally buoyant particles with small Stokes number), particles behave very similarly to tracers: they similarly sample the flow topology and their breakup is mostly dictated by the shear stress statistics. However, as soon as deviations from neutral buoyancy occur, inertial effects become dominant even at small Stokes numbers and have been seen to be able to cause the breakup of even the most resistant aggregates. A characterization of the flow topology seen by particles has also been conducted, and it agrees quantitatively with previously reported data for turbulence induced segregation.

Our investigation puts the basis for further developments for the measure and modeling of breakup due to shear and drag stresses. In fact, it can be considered as a first step towards the development of breakup kernels for inertial brittle aggregates. Laboratory and numerical investigations aimed at assessing the outcome of breakup events in terms of the fragment size distribution would complement our findings, and provide the full information needed for calibrating macroscopic population balance models addressing breakup in homogeneous solid-liquid turbulent flows.

Bäbler, M. U., Biferale, L., Brandt, L., Feudel, U., Guseva, K., Lanotte, A. S., Marchioli, C., Picano, F., Sardina, G., Soldati, A., & Toschi, F. (2015). Numerical simulations of aggregate breakup in bounded and unbounded turbulent flows. *Journal of Fluid Mechanics*, *766*, 104–128. doi:https://doi.org/10.1017/jfm.2015.13.

Bäbler, M. U., Biferale, L., & Lanotte, A. S. (2012). Breakup of small aggregates driven by turbulent hydrodynamical stress. *Phys. Rev. E*, *85*, 025301(R). doi:https://doi.org/10.1103/PhysRevE.85.025301.

Bäbler, M. U., Morbidelli, M., & Bałdyga, J. (2008). Modelling the breakup of solid aggregates in turbulent flows. *Journal of Fluid Mechanics*, *612*, 261–289. doi:https://doi.org/10.1017/S002211200800298X.

Bec, J., Biferale, L., Cencini, M., Lanotte, A. S., Musacchio, S., & Toschi, F. (2007). Heavy particle concentration in turbulence at dissipative and inertial scales. *Physical Review Letters*, *98*, 084502. doi:https://doi.org/10.1103/PhysRevLett.98.084502.

Bec, J., Biferale, L., Cencini, M., Lanotte, A. S., & Toschi, F. (2011). Spatial and velocity statistics of inertial particles in turbulent flows. *Journal of Physics: Conference Series*, *333*, 012003. doi:`https://doi.org/10.1088/1742-6596/333/1/012003`.

Bec, J., Biferale, L., Lanotte, A. S., Scagliarini, A., & Toschi, F. (2010). Turbulent pair dispersion of inertial particles. *Journal of Fluid Mechanics*, *645*, 497–528. doi:`https://doi.org/10.1017/S0022112009992783`.

Bec, J., Celani, A., Cencini, M., & Musacchio, S. (2005). Clustering and collisions of heavy particles in random smooth flows. *Physics of Fluids*, *17*, 073301. doi:`https://doi.org/10.1063/1.1940367`.

Boffetta, G., Celani, A., De Lillo, F., & Musacchio (2007). The eulerian description of dilute collisionless suspension. *Europhysics Letters*, *78*, 14001. doi:`https://doi.org/10.1209/0295-5075/78/14001`.

Brady, J. F., & Bossis, G. (1988). Stokesian dynamics. *Annual review of fluid mechanics*, *20*, 111–157. doi:`https://doi.org/10.1146/annurev.fl.20.010188.000551`.

Brandt, L., & Coletti, F. (2022). Particle-laden turbulence: Progress and perspectives. *Annual Review of Fluid Mechanics*, *54*, 159–189. doi:`https://doi.org/10.1146/annurev-fluid-030121-021103`.

Breuer, M., & Khalifa, A. (2019). Revisiting and improving models for the breakup of compact dry powder agglomerates in turbulent flows within Eulerianâ ĂŞLagrangian simulations. *Powder Technology*, *348*, 105–125. doi:`https://doi.org/10.1016/j.powtec.2019.03.009`.

Brouzet, C., Guiné, R., Dalbe, M.-J., Favier, B., Vandenberghe, N., Villermaux, E., & Verhille, G. (2021). Laboratory model for plastic fragmentation in the turbulent ocean. *Physical Review Fluids*, *6*, 024601. doi:`https://doi.org/10.1103/PhysRevFluids.6.024601`.

Calzavarini, E., Cencini, M., Lohse, D., Toschi, F. et al. (2008a). Quantifying turbulence-induced segregation of inertial particles. *Physical Review Letters*, *101*, 084504. doi:`https://doi.org/10.1103/PhysRevLett.101.084504`.

Calzavarini, E., Kerscher, M., Lohse, D., & Toschi, F. (2008b). Dimensionality and morphology of particle and bubble clusters in turbulent flow. *Journal of Fluid Mechanics*, *607*, 13–24. doi:`https://doi.org/10.1017/S0022112008001936`.

Capecelatro, J., Longest, W., Boerman, C., Sulaiman, M., & Sundaresan, S. (2022). Recent developments in the computational simulation of dry powder inhalers. *Advanced Drug Delivery Reviews*, *188*, 114461. doi:`https://doi.org/10.1016/j.addr.2022.114461`.

Chen, S., & Li, S. (2020). Collision-induced breakage of agglomerates in homogenous isotropic turbulence laden with adhesive particles. *Journal of Fluid Mechanics*, *902*. doi:`https://doi.org/10.1017/jfm.2020.582`.

Conchúir, B. O., & Zaccone, A. (2013). Mechanism of flow-induced biomolecular and colloidal aggregate breakup. *Physical Review E*, *87*, 032310. doi:`https://doi.org/10.1103/PhysRevE.87.032310`.

De Bona, J., Lanotte, A. S., & Vanni, M. (2014). Internal stresses and breakup of rigid isostatic aggregates in homogeneous and isotropic turbulence. *Journal of Fluid Mechanics*, *755*, 365âĂŞ396. doi:`https://doi.org/10.1017/jfm.2014.421`.

Falkovich, G., & Pumir, A. (2007). Sling effect in collisions of water droplets in turbulent clouds. *Journal of the Atmospheric Sciences*, *64*, 4497–4505. doi:`https://doi.org/10.1175/2007JAS2371.1`.

Frungieri, G., Bäbler, M. U., & Vanni, M. (2020a). Shear-induced heteroaggregation of oppositely charged colloidal particles. *Langmuir*, *36*, 10739–10749. doi:`https://doi.org/10.1021/acs.langmuir.0c01536`.

Frungieri, G., Boccardo, G., Buffo, A., Karimi-Varzaneh, H. A., & Vanni, M. (2022). CFD-DEM characterization and population balance modelling of a dispersive mixing process. *Chemical Engineering Science*, *260*, 117859. doi:`https://doi.org/10.1016/j.ces.2022.117859`.

Frungieri, G., Boccardo, G., Buffo, A., Marchisio, D., Karimi-Varzaneh, H. A., & Vanni, M. (2020b). A CFD-DEM approach to study the breakup of fractal agglomerates in an internal mixer. *The Canadian Journal of Chemical Engineering*, *98*, 1880–1892. doi:`https://doi.org/10.1002/cjce.23773`.

Frungieri, G., & Vanni, M. (2017). Shear-induced aggregation of colloidal particles: A comparison between two different approaches to the modelling of colloidal interactions. *The Canadian Journal of Chemical Engineering*, *95*, 1768–1780. doi:`https://doi.org/10.1002/cjce.22843`.

Frungieri, G., & Vanni, M. (2021). Aggregation and breakup of colloidal particle aggregates in shear flow: A combined Monte Carlo-Stokesian dynamics approach. *Powder Technology*, *388*, 357–370. doi:`https://doi.org/10.1016/j.powtec.2021.04.076`.

Garvey, C. J., Impéror-Clerc, M., Rouzière, S., Gouadec, G., Boyron, O., Rowenczyk, L., Mingotaud, A. F., & Ter Halle, A. (2020). Molecular-scale understanding of the embrittlement in polyethylene ocean debris. *Environmental Science & Technology*, *54*, 11173–11181. doi:`https://doi.org/10.1021/acs.est.0c02095`.

Gatignol, R. (1983). The Faxen formulae for a rigid particle in an unsteady non-uniform stokes flow. *Journal de Mécanique Theorique et Appliquée*, *1*, 143–160.

Guseva, K., & Feudel, U. (2017). Aggregation and fragmentation dynamics in random flows: From tracers to inertial aggregates. *Physical Review E*, *95*, 062604. doi:`https://doi.org/10.1103/PhysRevE.95.062604`.

Harada, S., Tanaka, R., Nogami, H., & Sawada, M. (2006). Dependence of fragmentation behavior of colloidal aggregates on their fractal structure. *Journal of Colloid and Interface Science*, *301*, 123–129. doi:`https://doi.org/10.1016/j.jcis.2006.04.051`.

Harshe, Y. M., & Lattuada, M. (2012). Breakage rate of colloidal aggregates in shear flow through stokesian dynamics. *Langmuir*, *28*, 283–292. doi:`https://doi.org/10.1021/la2038476`.

Jiang, Y., Alonso-Marroquín, F., Herrmann, H. J., & Mora, P. (2020). Particle fragmentation based on strain energy field. *Granular Matter*, *22*, 1–10. doi:`https://doi.org/10.1007/s10035-020-01038-6`.

Kusters, K. A. (1991). *The influence of turbulence on aggregation of small particles in agitated vessels*. Ph.D. thesis Technische Universiteit Eindhoven. doi:`https://doi.org/10.6100/IR362582`.

Lebaz, N., Azizi, F., & Sheibat-Othman, N. (2021). Modeling droplet breakage in continuous emulsification using static mixers in the framework of the entire spectrum of turbulent energy. *Industrial & Engineering Chemistry Research*, *61*, 541–553. doi:`https://doi.org/10.1021/acs.iecr.1c03529`.

Lehnigk, R., Bainbridge, W., Liao, Y., Lucas, D., Niemi, T., Peltola, J., & Schlegel, F. (2022). An open-source population balance modeling framework for the simulation of polydisperse multiphase flows. *AIChE Journal*, *68*, e17539. doi:`https://doi.org/10.1002/aic.17539`.

Lindgren, G. (2019). Gaussian integrals and Rice series in crossing distributionsâĂŤto compute the distribution of maxima and other features of Gaussian processes. *Statistical Science*, *34*, 100–128. doi:`https://doi.org/10.1214/18-STS662`.

Loginov, V. I. (1986). Dynamics of the process of breakup of a liquid in a turbulent system. *Journal of Applied Mechanics and Technical Physics*, *26*, 509. doi:`https://doi.org/10.1007/BF01101633`.

Maluta, F., Buffo, A., Marchisio, D., Montante, G., Paglianti, A., & Vanni, M. (2021). Effect of turbulent kinetic energy dissipation rate on the prediction of droplet size distribution in stirred tanks. *International Journal of Multiphase Flow*, *136*, 103547. doi:`https://doi.org/10.1016/j.ijmultiphaseflow.2020.103547`.

Marchioli, C., & Soldati, A. (2015). Turbulent breakage of ductile aggregates. *Physical Review E*, *91*, 053003. doi:`https://doi.org/10.1103/PhysRevE.91.053003`.

Marchisio, D. L., Soos, M., Sefcik, J., & Morbidelli, M. (2006). Role of turbulent shear rate distribution in aggregation and breakage processes. *AIChE journal*, *52*, 158–173. doi:`https://doi.org/10.1002/aic.10614`.

Maxey, M. R. (1987). The motion of small spherical particles in a cellular flow field. *Physics of Fluids*, *30*, 915âĂŞ1928. doi:`https://doi.org/10.1063/1.866206`.

Maxey, M. R., & Riley, J. J. (1983). Equation of motion of a small rigid sphere in a nonuniform flow. *Physics of Fluids*, *26*, 883âĂŞ889. doi:`https://doi.org/10.1063/1.864230`.

Poulain, M., Mercier, M. J., Brach, L., Martignac, M., Routaboul, C., Perez, E., Desjean, M. C., & Ter Halle, A. (2018). Small microplastics as a main contributor to plastic mass balance in the north atlantic subtropical gyre. *Environmental Science & Technology*, *53*, 1157–1164. doi:`https://doi.org/10.1021/acs.est.8b05458`.

Pumir, A., & Wilkinson, M. (2016). Collisional aggregation due to turbulence. *Annual Review of Condensed Matter Physics*, *7*, 141–170. doi:`https://doi.org/10.1146/annurev-conmatphys-031115-011538`.

Ruan, X., Chen, S., & Li, S. (2020). Structural evolution and breakage of dense agglomerates in shear flow and Taylor-Green vortex. *Chemical Engineering Science*, *211*, 115261. doi:`https://doi.org/10.1016/j.ces.2019.115261`.

Sabia, C., Casalini, T., Cornolti, L., Spaggiari, M., Frigerio, G., Martinoli, L., Martinoli, A., Buffo, A., Marchisio, D. L., & Barbato, M. C. (2022). A novel uncoupled quasi-3D Euler-Euler model to study the spiral jet mill micronization of pharmaceutical substances at process scale: Model development and validation. *Powder Technology*, *405*, 117573. doi:`https://doi.org/10.1016/j.powtec.2022.117573`.

Saha, D., Bäbler, M. U., Holzner, M., Soos, M., Lüthi, B., Liberzon, A., & Kinzelbach, W. (2016). Breakup of finite-size colloidal aggregates in turbulent flow investigated by three-dimensional (3D) particle tracking velocimetry. *Langmuir*, *32*, 55–65. doi:`https://doi.org/10.1021/acs.langmuir.5b03804`.

Scatamacchia, R., Biferale, L., & Toschi, F. (2012). Extreme events in the dispersions of two neighboring particles under the influence of fluid turbulence. *Physical Review Letters*, *109*, 144501. doi:`https://doi.org/10.1103/PhysRevLett.109.144501`.

Schikarski, T., Avila, M., Trzenschiok, H., Güldenpfennig, A., & Peukert, W. (2022). Quantitative modeling of precipitation processes. *Chemical Engineering Journal*, *444*, 136195. doi:`https://doi.org/10.1016/j.cej.2022.136195`.

Syed, A. H., Boulet, M., Melchiori, T., & Lavoie, J.-M. (2018). CFD simulation of a slurry bubble column: Effect of population balance kernels. *Computers & Fluids*, *175*, 167–179. doi:`https://doi.org/10.1016/j.compfluid.2018.07.009`.

Vasquez Giuliano, L., Buffo, A., Vanni, M., Lanotte, A. S., Arima, V., Bianco, M., Baldassarre, F., & Frungieri, G. (2022). Response of shear-activated nanotherapeutic particles in a clot-obstructed blood vessel by CFD-DEM simulations. *The Canadian Journal of Chemical Engineering*, *100*, 3562–3574. doi:`https://doi.org/10.1002/cjce.24502`.

Wang, L.-P., & Maxey, M. R. (1993). Settling velocity and concentration distribution of heavy particles in homogeneous isotropic turbulence. *Journal of Fluid Mechanics*, *256*, 27–68. doi:`https://doi.org/10.1017/S0022112093002708`.

Yao, Y., & Capecelatro, J. (2021). Deagglomeration of cohesive particles by turbulence. *Journal of Fluid Mechanics*, *911*, A10. doi:`https://doi.org/10.1017/jfm.2020.1020`.

Zaccone, A., Soos, M., Lattuada, M., Wu, H., Bäbler, M. U., & Morbidelli, M. (2009). Breakup of dense colloidal aggregates under hydrodynamic stresses. *Physical Review E*, *79*, 061401. doi:`https://doi.org/10.1103/PhysRevE.79.061401`.

Zahnow, J. C., Maerz, J., & Feudel, U. (2011). Particle-based modeling of aggregation and fragmentation processes: Fractal-like aggregates. *Physica D: Nonlinear Phenomena*, *240*, 882–893. doi:`https://doi.org/10.1016/j.physd.2011.01.003`.

Zhang, H., Wang, Y., Sayyar, A., & Wang, T. (2021). A CFD-PBM coupled model under entire turbulent spectrum for simulating a bubble column with highly viscous media. *AIChE Journal*, (p. e17473). doi:`https://doi.org/10.1002/aic.17473`.